Bridging spatiotemporal scales of normal fault growth during continental extension using high-resolution 3D numerical models

Sophie Pan[1*], John Naliboff[2], Rebecca Bell[1] and Chris Jackson[3]

[1]Department of Earth Science and Engineering, Imperial College, Prince Consort Road, London, SW7 2BP, UK

[2]Department of Earth and Environmental Science, New Mexico Institute of Mining and Technology, NM, USA

[3]Department of Earth and Environmental Sciences, The University of Manchester, Williamson Building, Oxford Road, Manchester, M13 9PL, UK

[*]Corresponding author: Sophie Pan (sophie.pan16@imperial.ac.uk)

Key Points:

- Normal fault growth is poorly understood due to the lack of spatial and temporally constrained observational datasets
- 3D numerical modelling reveal that fault patterns are rapidly established (<100 kyrs) and active deformation is highly transient
- Fault interaction and strain migration is crucial to understanding fault growth and their underpinning seismic hazards.

Abstract

Continental extension is accommodated by the development of kilometre-scale normal faults, which grow during metre-scale slip events that occur over millions of years. However, reconstructing the entire lifespan of a fault remains challenging due to a lack of observational data with spatiotemporal scales that span the early stage (<10^6 yrs) of fault growth. Using 3D numerical simulations of continental extension and novel methods for extracting the locations of faults, we quantitatively examine the key factors controlling the growth of rift-scale fault networks over 10^4-10^6 yrs. Early-formed faults (<100 kyrs from initiation) exhibit scaling ratios consistent with those characterising individual earthquake ruptures, before evolving to be geometrically and kinematically similar to more mature structures developed in natural fault networks. While finite fault lengths are rapidly established (<100 kyrs), active deformation is transient, migrating both along- and across-strike. Competing stress interactions determine the distribution of active strain, which oscillates locally between being localised and highly distributed. Higher rates of extension (10 mm yr^{-1}) lead to more prominent stress redistributions through time, promoting episodic localised slip events. Our findings demonstrate that normal fault growth and the related occurrence of cumulative slip is more complex than that currently inferred from displacement patterns on now-inactive structures, which only provide a spatial- and time-averaged picture of fault kinematics and related geohazard.

1. Introduction

Recent advances in geodetic measurements allow for high-resolution surface observations of crustal deformation (e.g., Elliott et al., 2016). Seismological and geodetic data from an individual earthquake can be inverted using modelled fault geometry to infer slip distribution and magnitude (e.g., Walters et al., 2018). These data show that individual earthquake rupture patterns are variable and complex, with events typically temporally and spatially clustered (e.g., Coppersmith, 1989; Nicol et al., 2006). Seismological, geodetic, and geomorphological (i.e., field) data also show that rupture lengths are often considerably shorter than finite fault lengths, and multiple segment ruptures during a single event can trigger surprisingly high-magnitude, hazardous earthquakes (7.9 M_w Kaikoura, New Zealand; Hamling et al., 2017; 7.2 M_w El Mayor-Cucapah, Mexico; Fletcher et al., 2014) that challenge the models underpinning seismic hazard assessments (Field et al., 2014).

Active seismogenic rifts (i.e., across the central Italian Apennines, East Mediterranean, Gulf of Corinth, Malawi, and Basin and Range) allow for slip rates to be constrained through the modelling of cosmogenic nuclides measured on bedrock scarps over intermediate (10^4-10^5 yr) timescales (e.g, Nixon et al., 2016; Shillington et al., 2020; Wedmore et al,. 2020). Increasingly, studies show that fault activity is episodic and slip rates are spatially and temporally variable (Friedrich et al., 2003; Schlagenhauf et al., 2008; Cowie et al., 2017). Studies focused on Holocene deformation show that metres of displacement accumulate rapidly in higher-than-average slip rates over several thousand years, separated by periods of lower-than-average slip rates and relative quiescence (Bennedetti et al., 2013; Mechernich et al., 2018; Goodall et al., 2021). The active rift record is short and provides only a temporal snapshot of the long, geological timescale over which faults grow. The way in which slip accumulates to produce the fault displacement patterns observed over geological time-scales thus remains poorly understood (e.g., Mouslopoulou et al., 2009).

Large (e.g., tens of kilometres long, several kilometres of displacement) normal faults grow by accumulating metre-scale co-seismic slip during earthquakes, and slow aseismic growth (creep) between earthquakes. Geometrical observations of faults are commonly used to understand how faults grow, typically using the empirical linear relationship between displacement (D) and length (L) (e.g., Cowie and Scholz 1992; Dawers et al., 1993; Walsh et al., 2002). Initially, D-L compilations observed in the field led to the proposition that fault lengths increase simultaneously with displacement through time (the propagating fault model; Walsh and Watterson, 1988). More recently, however, the analysis and age-dating of growth strata preserved adjacent to ancient faults imaged in 3D seismic data suggest that displacement accumulates on faults of near-constant length (the constant-length fault model; Walsh et al., 2002; Meyer et al., 2002). Both fault growth models imply systematic increases in slip accumulation, with fault displacement rates in ancient rifts found to be stable over long time periods of 1-40 Myrs (Nicol et al 1997), although this appears at odds with the variability observed in active rifts and earthquake behaviour, which are found to be irregular in slip rate, size, location and occurrence (e.g., Weldon et al., 2004). It is challenging to reconstruct fault growth over shorter timescales (<10^6 yrs) using observational data alone, principally due to: (i) limited seismic reflection data resolution in the subsurface; (ii) the lack of exposures of hanging wall growth strata in the field; and (iii) a lack of age-constraints on syn-kinematic (growth) strata in both subsurface and field data (Jackson et al., 2017).

Due to the lack of observational datasets of the appropriate temporal and spatial scale, it remains unclear how complex incremental slip patterns ultimately relate to the longer-term, relatively simple and stable pattern of displacement accumulation apparently characterising on large, mature faults. Here, we use high-resolution thermal-mechanical 3D simulations of continental extension to examine the evolution of normal fault networks across spatiotemporal scales poorly sampled by observational datasets (i.e., over 10^4-10^5 yr increments). Using novel image processing techniques, the active length, strain and cumulative strain are extracted from large fault populations across multiple timesteps and compared to natural D-L observations from active and ancient rifts, providing insights into the kinematics that constrain fault growth, and the underlying dynamics governing their evolution.

2. Numerical modelling of continental extension

2.1. Model setup

We use the open-source, mantle convection and lithospheric dynamics code ASPECT (Kronbichler et al., 2012; Heister et al., 2017) to model 3D continental extension (Fig. 1a). The governing equations are solved on a 3D gridded domain that spans 500 by 500 km across the horizontal plane (X, Y) and 100 km in the depth (Z) direction (Fig. 1a). The grids are coarsest (5 km) on the sides and base of the model domain and are successively reduced using adaptive-mesh refinement, increasing the resolution to 625 m over a central region measuring 180 x 180 x 20 km (Fig. 1a). Broadly, this approach provides 'natural' boundary conditions for the formation of a distributed fault network within the upper crust.

Orthogonal extension is driven by prescribed outflow velocities on the left and right sides, with inflow at the model base exactly balancing the outflow. The top of the model is a free surface (Rose et al., 2015) and is advected normal to the velocity field. We model extension rates (i.e., the prescribed outward velocity) of 2.5, 5 or 10 mm yr^{-1}, which correspond to the range of values widely used in prior numerical simulations of continental extension (e.g., Van Wijk 2002;

Naliboff et al., 2020) and are comparable to those characterising active rifts (e.g., Argus and Helflin 1995; Bell et al., 2011).

2.2. Governing equations

The model solves the conservation of momentum, mass and energy equations, combined with advection-diffusion equations, which are outlined below. The Stokes equation that solves for velocity and pressure are defined as:

$$\nabla \cdot \boldsymbol{u} = 0 \tag{1}$$

$$-\nabla \cdot 2\,\mu\,\dot{\varepsilon}(\boldsymbol{u}) + \nabla p = \rho \boldsymbol{g} \tag{2}$$

Where $\boldsymbol{u}$ is the velocity, μ is the viscosity, $\dot{\varepsilon}$ is the second deviator of the strain rate tensor, p is pressure, ρ is density, and $\boldsymbol{g}$ is gravitational acceleration.

Temperature evolves through a combination of advection, heat conduction, shear heating, and adiabatic heating:

$$\rho C_p \left(\frac{\partial T}{\partial t} + \boldsymbol{u} \cdot \nabla T\right) - \nabla \cdot \left(\kappa \rho C_p\right) \nabla T = \rho H + 2\eta\,\dot{\varepsilon}(\boldsymbol{u}) + -\alpha \rho T \boldsymbol{u} \cdot g \tag{3}$$

Where C_p is the heat capacity, T is temperature, t is time, κ is thermal diffusivity, α is the linear thermal expansion coefficient, and H is the rate of internal heating. Respectively, the terms on the right-hand side correspond to internal head production, shear heating, and adiabatic heating.

Density varies linearly as a function of the reference density (ρ_0), linear thermal expansion coefficient (α), reference temperature (T_0), and temperature:

$$\rho = \rho_0 \left(1 - \alpha \left(T - T_0\right)\right) \tag{4}$$

2.3. Initial conditions

The model domain contains three distinct compositional layers, representing the upper crust (0-20 km depth), lower crust (20-40 km depth), and lithospheric mantle (40-100 km depth). Distinct background densities (2700, 2800, 3300 kg m^{-3}) and viscous flow laws for dislocation creep (wet quartzite; Gleason and Tullis, 1995, wet anorthite; Rybacki et al., 2003, dry olivine; Hirth and Kohlstedt, 2003) distinguish these three layers, which deform through a combination of nonlinear viscous flow and brittle (plastic) deformation (e.g., Glerum et al., 2018; Naliboff et al., 2020; Gouiza and Naliboff, 2021). Table 1 contains the specific parameters for each flow law.

The initial temperature distribution follows a characteristic conductive geotherm for the continental lithosphere (Chapman, 1986). We solve for the conductive profile by first assuming a thermal conductivity of 2.5 W m^{-1} K^{-1}, a surface temperature of 273 K, and a surface heat flow of 55 mW/m2, and constant radiogenic heating in each compositional layer (Table 1) that we use to calculate the temperature with depth within each layer. The resulting temperature at the base of the upper crust, lower crust, and mantle lithosphere are 633, 893, and 1613 ^{o}K, respectively.

2.4. Rheological formulation

Rheological behaviour combines nonlinear viscous flow with brittle failure (see Glerum et al., 2018). Viscous flow follows dislocation creep, formulated as:

$$\sigma'_{II} = A^{-\frac{1}{n}} \, \dot{\varepsilon}_{II}^{\frac{1}{n}} \, e^{\frac{Q+P\,V}{n\,R\,T}} \tag{5}$$

Above, σ'_{II} is the second invariant of the deviatoric stress, A is the viscous prefactor, n is the stress exponent, $\dot{\varepsilon}_{II}$ is the second invariant of the deviatoric strain rate (effective strain rate), Q is the activation energy, P is pressure, V is the activation volume, T is temperature, and R is the gas constant

Brittle plastic deformation follows a Drucker Prager yield criterion, which accounts for softening of the angle of internal friction (ϕ) and cohesion (C) as a function of accumulated plastic strain:

$$\sigma'_{II} = \frac{6\,C\ \cos\phi + \ 2\,P\ \sin\phi}{\sqrt{(3)}(3\ +\ \sin\phi)} \tag{6}$$

The initial friction angle and cohesion are 30 and 20 MPa respectively, and linearly weaken by a factor of 2 as a function of finite plastic strain. Rather than a single weak seed (e.g., Lavier et al., 2000; Huismans et al., 2007), or randomised distribution at each grid point (e.g., Naliboff et al., 2020; Duclaux et al., 2020; Gouiza and Naliboff, 2021), initial plastic strain is partitioned into 5 km coarse blocks that are randomly assigned a strong (0.5) or weak (1.5) value. This results in statistically random but pervasive damage, which from a geological perspective may reflect the structural heterogeneity observed in many natural systems, where deformation exploits inherited weaknesses such as pervasive fabrics (e.g., Phillips et al., 2016) or the margins of strong zones (e.g., ancient cratons; e.g., Dunbar and Sawyer, 1989). Critically, the use of a randomised initial plastic strain field decoupled from the numerical resolution produces significantly faster localisation of a well-defined normal fault network (Fig. 1b) relative to recent studies that defined randomised plastic strain at each grid point, and which used a continuous randomised value range rather than a binary distribution (e.g., Naliboff et al., 2020; Gouiza and Naliboff, 2021).

The viscosity is calculated using the viscosity rescaling method, where if the viscous stress exceeds plastic yield stress, the viscosity is reduced such that the effective stress matches the plastic yield (see Glerum et al., 2018). Nonlinearities from the Stokes equations are addressed by applying defect-Picard iterations (Fraters et al., 2019) to a tolerance of 1e-4. The maximum numerical time step is limited to 20 kyrs.

3. Automated fault extraction workflow

To quantitatively analyse the geometry and kinematics of faults throughout the entire model, automated fault identification and extraction is required. Previous applications towards geodynamic fault extraction (Duclaux et al., 2020; Naliboff et al., 2020) utilise conventional image processing techniques such as thresholding (where data is removed at a defined cut-off value) and labelling (where pixels connected to neighbouring pixels are labelled as a number e.g., Dillencourt et al., 1992) (Fig. 2). However, manually defined thresholds may introduce biases to a fault's length and does not retain the complex fault interactions forming the focus of this study (Fig. 2)

Here, the strain rate field is sampled on a horizontal plane located 5 km beneath the initial model surface as the extent of the fault network is captured at this depth (Fig. 3a). We derived the strain rate field along the longitudinal (along-strike) direction and equalised the resulting field to capture small-scale faulting and allow for a consistent global extraction across other timesteps (Fig. 3b). Large differences across-strike are extracted from Fig. 3b to produce a binary image (Fig. 3c), which is then labelled (Dillencourt, 1992) such that each identified fault has a unique, accessible index (Fig. 3e). Noise is filtered out by removing fault labels that contain less than 20 points. This approach largely recovers detailed interactions between distinct active fault strands, remaining continuous along consistent strain rate magnitudes, and segmenting at abrupt decreases in strain rate (Fig. 3e).

Geometric attributes such as fault length and displacement are extracted by iterating through each label. Labels are thinned to a pixel length and fault length is computed using the cumulative euclidean distance (Fig. 3f). On a few occasions the calculated euclidean distance is abnormally high as the fault splay along-strike, therefore the localities of erroneous distances are used to split labels into discrete fault segments at the point of bifurcation. The locality of the fault label is masked over the cumulative strain field to extract the maximum strain occupied by that label. Strain is converted to displacement by multiplying by 2x the grid resolution (625 m), as on average, shear bands typically span two elements.

4. Model Results

The evolution of the modelled fault network for a 5 mm yr^{-1} extension rate is shown in Fig. 4. The network contains faults of varying lengths (c. 5-200 km), which often exhibit along-strike changes in strike, and that may splay and link with adjacent structures (Fig. 4). Fault patterns and specifically length, are established during the first modelled timestep, thus fault appears to grow in accordance with the ‘constant-length’ model (Movie S1). For the remainder of extension, strain accumulates such that finite strain patterns (i.e., displacement) exhibit strain maxima that are typically located near the map-view centres of individual fault systems (e.g., Pollard and Seagall 1980; Cowie and Shipton, 1998; Kim and Sanderson, 2005; Fig. 4, Movie S1). The along-strike variability in finite strain is comparable to that observed in active natural systems in the field (e.g., Nixon et al., 2016; Mildon et al., 2017; Faure-Walker et al., 2021) and in ancient rifts studied using seismic reflection datasets (e.g., McLeod et al., 2010; Reeve et al., 2015). The strain rate (Fig. 5a-c) and extracted active fault locations (Fig. 5d-f) for models with extension rates of 2.5, 5, or 10 mm yr^{-1} reveal active deformation accommodated on complex fault networks. Our results show that the spatial pattern of the fault network appears similar across the investigated models; however in models with faster extension rates, the overall magnitude of strain rate increases and is accommodated across increasingly diffuse zones of deformation (Fig. 5a, c, e).

The finite displacement-length (D-L) ratios for individual faults within the modelled network are geometrically similar, based on global D-L compilations, to those identified in natural systems (Fig. 6) (e.g., Walsh and Watterson, 1991; Kim and Sanderson, 2005). During the earliest stages of rifting, i.e., within the first resolvable timestep (c. 200, 100 and 50 kyrs for extension rates of 2.5, 5, or 10 mm yr^{-1}, respectively), active deformation is accommodated along distributed fault networks (Fig. 4a and b; Movie S1 and 2) that are similar in appearance to their finite fault patterns (Fig. 4c and d). During this earliest timestep (<100 kyrs) the faults are seemingly under-displaced compared to geological D-L datasets, instead plotting on the slip-length ratio associated with individual earthquakes (c = 0.00005 from Wells and Coppersmith, 1994; Li et al 2012; Manighetti et al., 2009; Wesnousky, 2008; Baize et al., 2020; Fig. 6). Again, this geometric characteristic is consistent with the constant-length fault model. The modelled D-L relationships show significant scatter (over 2-3 orders of magnitude) throughout each model timestep, similar to magnitudes observed from ancient and active fault D-L studies. The scatter may be attributed to the process of fault growth, rather than measurement errors or variation in mechanical properties (Cartwright et al., 1995; Pan et al., 2021) and may reflect how individual earthquakes accumulate displacement over intermediate (10^3–10^6 yr) timescales (Mouslopoulou et al., 2009; Nicol et al., 2009, 2010, 2020).

Time-series of the total number of active faults (Fig. 7), and the average fault length in a given population (Fig. 7b), reveal significant fluctuations throughout time. All three models (with extensions rates of 2.5, 5, 10 mm yr^{-1}) show an increase in fault number and average fault length within the first c. 10 timesteps (Fig. 7), corresponding to a transition from an initially diffuse fault pattern which rapidly localises (i.e., reduces in element width) within the first few timesteps (see Movie S1-2, 4-6). Both the total number of faults and mean length continue to fluctuate throughout the remainder of extension, reflecting oscillations between localised and distributed active deformation throughout the crust (Fig. 7). This behaviour is consistent with spatiotemporal clustering of earthquakes promoted by stress interactions between neighbouring faults (Stein 1999). In comparison to the 2.5 and 5 mm yr^{-1} models, the oscillations in fault number and active lengths (Fig. 7) in the 10 mm yr^{-1} model are greater, and its notably different pattern of active deformation (Fig. 5e-f) indicate that increases in extension rate consequently produce more prominent stress redistributions through time. After an initiation phase of 0.5 Myrs in the 10 mm yr^{-1} model, the mean active lengths episodically reach highs of c. 20 km and lows of c. 15 km across recurrence intervals of c. 350 kyrs (Fig. 7). Although transient behaviour continues for the remainder of extension, the overall number of faults decreases across all models and the average fault length slightly increases (Fig. 7), demonstrating that large-scale localisation occurs as strain is concentrated onto fewer, larger fault systems (e.g., Cowie, 1998).

Transient deformation occurs both along- and perpendicular to the rift axis, which we view in a regional model subset (Movie S4-6). This subset shows along-strike migration of deformation (Movie S7) consistent with the preferential along-strike propagation direction of (eventual) plate rupture. The across-strike strain migration correlates to along-strike bends (Movie S4-6), supporting observations from active settings that earthquakes commonly occur at segment boundaries (DuRoss et al., 2016), and that relay ramps may be associated with throw rate enhancements (Faure-Walker et al., 2009; Iezzi et al., 2018). The behaviour of transient strain migration appears similar to the proposal of clustered earthquake activity that migrates through time in the Basin and Range (Wallace, 1987). Overall, both along- and across- strike strain migration, reflective of competing stress-interactions between faults in the near field (e.g., Cowie, 1998) as documented in Fig. 7, produce end-member behaviours characterised by localised, continuous slip (Fig. 8a-c) and distributed, segmented slip (Fig. 8d-f). This transient behaviour evolves without explicitly modelling the earthquake cycle via a rate or rate-state friction type rheology (e.g., Van Dinther et al., 2013), suggesting that the recurrence of large, clustered slip (e.g., Fig. 8a) can be produced by fault interaction and stress transfer within fault networks deforming at constant rates of tectonic extension. Faster extension rates (10 mm yr^{-1}) result in greater fluctuations between the aforenoted endmembers (Fig. 7), resulting in sudden, large, recurring through-going slip events (Fig. 8).

5. Discussion

The numerical models presented here exhibit establishment of near-maximum finite fault lengths from the onset of extension, consistent with the constant-length model (e.g, Walsh et al., 2002; Rotevatn et al., 2019). Faults therefore predominantly accumulate displacement (rather than length) through time and move upwards in D-L space, behaviour which clearly diverges from the linear relationship derived from observational D-L data which has historically underpinned the propagating fault model (Fig. 6) (Mansfield and Cartwright, 2001; Walsh et al,. 2002). Our results show that fault lengths are established an order of magnitude (<100 kyrs) earlier than currently inferred from seismic reflection analysis of ancient (c. 1.3 Myrs, NW Shelf, Australian; Walsh et al., 2002) and active (c. 700 kyrs, Whakatane Graben, New Zealand; Taylor et al., 2004) rifts. Fig. 6 shows that the D-L of early modelled fault networks plot below the scatter characterising existing observational compilations (where D/L = 0.001) and begin to lie largely within the observational scatter after 1 Myrs (Movie S3). This suggests that although the modelled faults rapidly formed their lengths within the first 100 kyrs, the initial 1 Myrs of fault lengthening may not be captured due to the resolution threshold of observational data used (i.e., seismic, field).

The constant-length model was initially proposed for faults that reactivated underlying pre-existing weaknesses (Walsh et al., 2002; Meyer et al., 2002). Our models indicate that the complex fault patterns manifested here reflect both the randomisation of the initial plastic strain field and the mechanical and kinematic interaction between adjacent faults. Our results thus suggest that the rapid establishment of fault patterns may arise in pervasively damaged crust, and does not necessarily require reactivation of a well-developed, pre-existing fault network. These findings are consistent with descriptions of basin-bounding faults in the East African Rift, which rapidly propagated without invoking the reactivation of pre-existing structures (Morley, 1999).

Distinguishing between currently debated fault growth models has direct implications for the nature of earthquake slip and potential maximum moment magnitude. As earthquake magnitudes are proportional to their rupture length, the propagating fault model would require a progressive temporal increase in the maximum earthquake magnitude and a decrease in recurrence for constant slip rates, whereas the constant-length model with constant slip rates can arise from invariant earthquake magnitude and recurrence (Nicol et al., 2005). Whereas our results demonstrate that finite fault lengths were rapidly established (i.e., constant-length model), they do not explicitly support either of the two slip models, instead showing that active deformation is temporally and spatially variable (i.e., earthquake slip is variable, not uniform, in magnitude and location), an observation consistent with episodic slip patterns characterising active fault networks (e.g., Mitchell et al., 2001; Benedetti et al., 2002; Friedrich et al., 2003; Nicol et al., 2006; Oskin et al., 2007; Schlagenhauf, 2008, 2010, 2011)

While the transient nature of active deformation exhibits short-term variability, the finite plastic strain field visually appears to accumulate strain at near-constant rates (i.e., long-term stability). Note that the finite plastic strain field appears identical at 2.1 and 2.2 Myrs (Fig. 8b and e) even though incremental slip (Fig. 8a and d) occurred. We suggest that short-term variability and long-term stability of strain accumulation depend on how deformation is spatially and temporally averaged. As the area in which deformation is summed increases, the strain rate profile along the rift axis becomes increasingly uniform as strain deficits in one location are compensated for by increased strain in other, across-strike locations (Movie S7). Rift-wide strain profiles (i.e., the summation of deformation across the analysed model in Fig. 5) result in constant rates directly proportional to the extensional velocity applied to the crust. The increased stability of strain rates at greater spatial scales supports the discussion of Nicol et al., (2006), which suggest that each fault is a component of a kinematically coherent system, in which all faults interact and have interdependent earthquake histories. Our results suggest that a kinematically coherent system is established from the onset of extension, giving rise to the rapid establishment of the fault pattern observed in the models (e.g., Fig. 4, 5).

The accommodation of small-scale strain that leads to the accumulation of overall uniform strain may highlight sampling bias limitations. A temporal bias may occur, given that measured slip rates are more likely to be obtained from episodic fault activity akin to the ‘localised’ endmember shown from the model results, rather than interseismic periods of aseismic slip, diffuse deformation, and relative quiescence (i.e., the distributed endmember in Fig. 8d-f) which are less likely to be recorded. Alternatively, a spatial bias may occur as it may be more likely that only the most prominent fault scarps mapped (e.g., Nicol et al., 2009) and only the largest faults interpreted in seismic data (e.g., Pan et al., 2021), as discussed by Cowie et al (2012). Small-scale, distributed deformation in the form of near-fault drag folding can account for 30% greater geodetic slip rates (Oskin, 2007). We suspect measured rates of slip in our models could be higher if the spatial scale of observation is able to recover all distributed deformation, particularly at higher extension rates (10 mm yr^{-1}) where distributed deformation is relatively widespread throughout the crust (Fig. 5).

Our results suggest that conventional D-L profiles measured for static fault geometries may provide only a limited understanding of fault growth, given they do not capture stress- and -time dependent stress interactions crucial to revealing the short- to intermediate-timescale variations in faulting that control earthquake magnitude and location. Our work suggests that a better understanding of fault interaction and stress feedback mechanisms are crucial to understanding and potentially forecasting patterns of fault growth and slip accumulation. Further observational data that capture strain migration (most likely in active rift settings) may therefore better constrain the mechanisms of stress feedback and subsequent geohazards. Additional modelling coupled to high-resolution geomorphology and surface processes may further enable our practical understanding of slip distribution and recurrence.

6. Conclusions

Numerical models of continental extension allow for a better understanding of normal fault growth via incremental slip accumulation. Fault lengths are established from the onset of extension (<100 kyrs from initiation) due to competing stress interactions from an initially randomised distribution of plastic strain. Subsequent strain accumulation is highly transient and active deformation oscillates between being localised and distributed throughout the crust. Our findings demonstrate that fault network evolution is more complex than currently inferred from observing finite displacement patterns on now-inactive structures (i.e., finite strain in Fig. 5b and e appear nearly identical), which provide only a time-averaged picture of fault kinematics. Short-term slip rates subsequently capture a transient snapshot of the long-term average. We suggest that short-term slip rates coupled to a better understanding of fault interaction and strain migration may greatly benefit our overall understanding of fault network evolution and their underpinning seismic hazards.

Data availability

The parameter file and additional inputs required to reproduce the models results are provided in the supplementary material. Models were run with ASPECT 2.2.0-pre with deal.II 9.1.1 on 720 processors (15 nodes). This version of ASPECT can be obtained with git checkout ab5eead39 from the main branch. We have also provided the extracted fault data for each model run as a supplementary file (S5).

Code availability

The Python code used for the automated data analysis and generating figures are included as supplementary files and are also available on the github repository described above. The software used to generate the initial composition field (S1) and geothermal profile (S2) are included as supplementary files, and described in the supplementary text.

Acknowledgements

PhD work is funded by Natural Environment Research Council (NERC) Centre for Doctoral Training (CDT) in Oil and Gas (NE/R01051X/1). The computational time for these simulations was provided under XSEDE project EAR180001.

Figure captions

Fig. 1. (a) Continental extension model setup outlining initial boundary conditions, compositional layers and prescribed initial strain. Resolution is progressively refined to higher levels up to 650 m in the model centre (180 x 180 x 20 km region), where we perform fault extraction analysis at 5 km beneath the initial model surface (e.g., 95 km above the model base). **(b)** Strain rate second invariant (1/s) after 100 kyrs, cropped to the centered 650 m resolution zone. The deformation patterns reveal that the randomised initial plastic strain field produces rapid localisation of a well-defined normal fault network.

Fig. 2. Conventional image processing techniques, which here are derived from the strain rate field 5 km below the initial model surface. This approach performs a binay threshold, where values below a specified cutoff point (3e-15 and 1-e15 1/s) are assigned 0 and values above are assigned 1 (**b** and **e**). Regions which are connected in the binary threshold are grouped into components labelled as integers (**c** and **f**). However, a high cutoff value does not capture small scale strain and makes fundamental assumptions on the resulting fault length (**c**). In contrast, a low cutoff value results in labels containing multiple fault segments, in which length cannot be

extracted (**f**). **Details and examples of this fault extraction procedure are provided in the supplementary materials.**

Fig. 3. Novel fault extraction workflow. The active deformation field (e.g., second strain invariant) is extracted 5 km below the initial model surface (a). The spatial derivative of the second strain invariant in the along-strike direction (e.g., z-direction) is calculated, and the resulting field is equalised to 0-1 showing that values of 0 and 1 lie on the sides of fault localities **(b)**. An across-strike derivation **(c)** identifies these localities, in which a binary threshold is applied **(d)**. Spatially connected regions of the binary array are labelled as integers **(e)** and noise is removed. This method results in the extraction of discrete fault segments, such that fault length may be derived **(f)**. **Details and examples of the novel fault extraction are provided in the supplementary materials.**

Fig. 4. Active deformation (left) and accumulated brittle plastic deformation (right) for the model extending a constant rate of 5 mm yr^{-1}, after 1 Myrs (**a** and **b**) and 5 Myrs (**c** and **d**) of extension. The second strain rate invariant (1/s) on the left, documenting active deformation, are limited to values above 1e-16 here to better reveal and compare the main active structures. At 1 Myr, deformation is relatively distributed across faults whereas at 5 Myrs structures are localised onto the largest faults. See Movie S1 for animation across all modelled timesteps.

Fig. 5. Comparison across models with extension rates of 2.5, 5, and 10 mm yr^{-1}. The top row shows the strain rate invariant (s^{-1}) in the upper crust (extracted at 5 km depth), documenting active deformation patterns within the last resolvable time increment (50) representing 10, 5 and 2.5 Myrs extension, respectively. The bottom row shows their corresponding fault length extracted from the active deformation field. See Movie S2 for animation across all modelled timesteps.

Fig. 6. Fault D-L evolution for the modelled fault network extending at a rate of 5 mm yr^{-1}. Observational datasets are plotted in grey, where different shades correlate to references therein, and the modelled data are in colour. See Movie S3 for animation across all modelled timesteps.

Fig. 7. Geometric statistics of time-dependent fault properties. (**a)** The number of active faults through time. **(b)** The average active fault length through time. Note that while the plot contains all output timesteps for each model (50 total), however the total duration for models deformed at 2.5, 5 and 10 mm yr^{-1} are 10, 5 and 2.5 Myrs, respectively. As such, each timestep along the horizontal axis corresponds to an equivalent amount of total extension experienced by each model, rather than the same model time.

Fig. 8. End-member behaviour of transient deformation. Along-strike maps from a subset of the model that experienced 10 mm yr^{-1} extension. The strain rate second invariant **(a)**, finite strain (plastic strain invariant) **(b)**, and extracted faults **(c)** at 2.1 Myrs reveal localised, continuous behaviour. The strain rate second invariant **(d)**, finite strain **(e)** and extracted faults **(f)** at 2.2 Myrs reveal distributed, segmented behaviour.

Supplementary Movies

Movie S1. Fault network evolution for the model undergoing extension at a rate of 5 mm/yr extension rates (see Fig. 1). Active deformation (left) and accumulated brittle plastic deformation (right) after 1 Myrs (**a** and **b**) and 5 Myrs (**c** and **d**). The strain rate invariant (1/s) on the left, documenting active deformation, are limited to values above 1e-16 here to better reveal and compare the main active structures. At 1 Myrs, deformation is relatively distributed across faults whereas at 5 Myrs structures are localised onto the largest faults.

Movie S2. Model evolution and **c**omparison across 2.5, 5, and 10 mm yr^{-1} extension rates. The top row shows the strain rate second invariant (s^{-1}) in the upper crust (extracted at 5 km depth relative to the initial model surface), documenting active deformation patterns within the last resolvable time increment (50) representing 10, 5 and 2.5 Myrs, respectively. The bottom row shows their corresponding fault length extracted from the active deformation field.

Movie S3. Animation of modelled D-L statistics through time for the model that underwent 5 mm/yr extension. Each step contains the extraction of the entire fault population at a given point in time.

Movie S4. Regional subsection of the 2.5 mm/yr extension model in order to focus on evolution across a single large fault system. The top panel shows the active deformation (strain rate), the middle panel shows cumulative finite plastic strain, and the lower panel shows the extracted faults coloured by their length (km).

Movie S5. Regional subsection of the 5 mm/yr extension model in order to focus on evolution across a single large fault system. The top panel shows the active deformation (strain rate), the middle panel shows cumulative finite plastic strain, and the lower panel shows the extracted faults coloured by their length (km).

Movie S6. Regional subsection of the 10 mm/yr extension model in order to focus on evolution across a single large fault system. The top panel shows the active deformation (strain rate), the middle panel shows cumulative finite plastic strain, and the lower panel shows the extracted faults coloured by their length (km).

Movie S7. Strain profiles across the regional subsection of the 10 mm/yr model. Here, active deformation is summed latitudinally across increasing spatial scales (from 3 to 1). Note that we sum the entire strain rate field, rather than from extracted faults. This shows that large spatial variations become increasingly uniform as scales increase.

Supplementary Material

Supplementary Material 1. Initial compositional field and the python script used to generate the input file, where plastic strain values of 1.5 and 0.5 are statistically distributed as blocks within the upper crust. Note that each run of the python script produces a new statistically random field.

Supplementary Material 2. Python script used to generate the geothermal profile

Supplementary Material 3. ASPECT parameter file (.prm) for 3D continental extension

Supplementary Material 4. Python script (fault_extraction_analysis.py) used to generate fault extraction workflow from the raw vtk data for timestep 50. Two jupyter notebooks provide a visual step-by-step instruction of how to first produce extracted faults from vtk data, and secondly reproduce the publication figures.

Supplementary Material 5. The python script (fault_extraction_analysis.py) produces statistical fault database for each model (‘Geometric relationships.xlsx) recording the length, maximum displacement, total strain, strike and coordinates for each fault. Here the fault statistics are attached for 2.5, 5 and 10 mm/yr extension models.

References

1. Argus, D. F., & Heflin, M. B. (1995). Plate motion and crustal deformation estimated with geodetic data from the Global Positioning System. *Geophysical Research Letters*, *22*(15), 1973-1976.
2. Baize, S., Nurminen, F., Sarmiento, A., Dawson, T., Takao, M., Scotti, O., et al. (2020).
3. Bell, R.E., McNeill, L.C., Henstock, T.J. and Bull, J.M., 2011. Comparing extension on multiple time and depth scales in the Corinth Rift, Central Greece. *Geophysical Journal International*, *186*(2), pp.463-470.
4. Benedetti, L., Finkel, R., Papanastassiou, D., King, G., Armijo, R., Ryerson, F., et al. (2002). Post-glacial slip history of the Sparta fault (Greece) determined by 36Cl cosmogenic dating: Evidence for non-periodic earthquakes. *Geophysical Research Letters*, *29*(8), doi: 10.1029/2001GL014510. https://doi.org/10.1029/2001GL014510
5. Benedetti, L., Manighetti, I., Gaudemer, Y., Finkel, R., Malavieille, J., Pou, K., et al. (2013). Earthquake synchrony and clustering on Fucino faults (Central Italy) as revealed from in situ 36 Cl exposure dating. *Journal of Geophysical Research: Solid Earth*, *118*(9), 4948–4974. https://doi.org/10.1002/jgrb.50299
6. Benedetti, L., Manighetti, I., Gaudemer, Y., Finkel, R., Malavieille, J., Pou, K., ... & Keddadouche, K. (2013). Earthquake synchrony and clustering on Fucino faults (Central Italy) as revealed from in situ 36Cl exposure dating. *Journal of Geophysical Research: Solid Earth*, *118*(9), 4948-4974.
7. Cartwright, J. A., Trudgill, B. D., & Mansfield, C. S. (1995). Fault growth by segment linkage: an explanation for scatter in maximum displacement and trace length data from the Canyonlands Grabens of SE Utah. *Journal of structural Geology*, *17*(9), 1319-1326.
8. Chapman, D.S., 1986. Thermal gradients in the continental crust. *Geological Society, London, Special Publications*, *24*(1), pp.63-70.
9. Coppersmith, K.J. and Youngs, R.R., 1989. Issues regarding earthquake source characterization and seismic hazard analysis within passive margins and stable continental interiors. In *Earthquakes at North-Atlantic Passive Margins: Neotectonics and Postglacial Rebound* (pp. 601-631). Springer, Dordrecht.
10. Cowie, P. A., & Scholz, C. H. (1992). Physical explanation for the displacement-length relationship of faults using a post-yield fracture mechanics model. *Journal of Structural Geology*, *14*(10), 1133-1148.
11. Cowie, P. A., & Shipton, Z. K. (1998). Fault tip displacement gradients and process zone dimensions. *Journal of Structural Geology*, *20*(8), 983-997.
12. Cowie, P. A., Phillips, R. J., Roberts, G. P., McCaffrey, K., Zijerveld, L. J. J., Gregory, L. C., et al. (2017). Orogen-scale uplift in the central Italian Apennines drives episodic behaviour of earthquake faults. *Sci. Rep.*, *7*(November 2016), 1–10. https://doi.org/10.1038/srep44858

13. Cowie, P.A., 1998. A healing–reloading feedback control on the growth rate of seismogenic faults. *Journal of Structural Geology*, *20*(8), pp.1075-1087.
14. Dawers, N. H., Anders, M. H., & Scholz, C. H. (1993). Growth of normal faults: Displacement-length scaling. *Geology*, *21*(12), 1107-1110.
15. Dawers, N.H. and Underhill, J.R., 2000. The role of fault interaction and linkage in controlling synrift stratigraphic sequences: Late Jurassic, Statfjord East area, northern North Sea. *AAPG bulletin*, *84*(1), pp.45-64.
16. Dillencourt, M.B., Samet, H. and Tamminen, M., 1992. A general approach to connected-component labeling for arbitrary image representations. *Journal of the ACM (JACM)*, *39*(2), pp.253-280.
17. Dixon, T.H., Norabuena, E. and Hotaling, L., 2003. Paleoseismology and Global Positioning System: Earthquake-cycle effects and geodetic versus geologic fault slip rates in the Eastern California shear zone. *Geology*, *31*(1), pp.55-58.
18. Duclaux, G., Huismans, R.S. and May, D.A., 2020. Rotation, narrowing, and preferential reactivation of brittle structures during oblique rifting. *Earth and Planetary Science Letters*, *531*, p.115952.
19. Dunbar, J.A. and Sawyer, D.S., 1989. How preexisting weaknesses control the style of continental breakup. *Journal of Geophysical Research: Solid Earth*, *94*(B6), pp.7278-7292.
20. DuRoss, C.B., Personius, S.F., Crone, A.J., Olig, S.S., Hylland, M.D., Lund, W.R. and Schwartz, D.P., 2016. Fault segmentation: New concepts from the Wasatch fault zone, Utah, USA. *Journal of Geophysical Research: Solid Earth*, *121*(2), pp.1131-1157.
21. Elliott, J.R., Walters, R.J. and Wright, T.J., 2016. The role of space-based observation in understanding and responding to active tectonics and earthquakes. *Nature communications*, *7*(1), pp.1-16.
22. Faure Walker, J., Boncio, P., Pace, B., Roberts, G., Benedetti, L., Scotti, O., et al. (2021). Fault2SHA Central Apennines database and structuring active fault data for seismic hazard assessment. *Scientific Data*, *8*(1), 87. https://doi.org/10.1038/s41597-021- 00868-0
23. Field, E.H., Arrowsmith, R.J., Biasi, G.P., Bird, P., Dawson, T.E., Felzer, K.R., Jackson, D.D., Johnson, K.M., Jordan, T.H., Madden, C. and Michael, A.J., 2014. Uniform California earthquake rupture forecast, version 3 (UCERF3)—The time-independent model. *Bulletin of the Seismological Society of America*, *104*(3), pp.1122-1180.
24. Fletcher, J.M., Teran, O.J., Rockwell, T.K., Oskin, M.E., Hudnut, K.W., Mueller, K.J., Spelz, R.M., Akciz, S.O., Masana, E., Faneros, G. and Fielding, E.J., 2014. Assembly of a large earthquake from a complex fault system: Surface rupture kinematics of the 4 April 2010 El Mayor–Cucapah (Mexico) Mw 7.2 earthquake. *Geosphere*, *10*(4), pp.797-827.
25. Fraters, M.R., Bangerth, W., Thieulot, C., Glerum, A.C. and Spakman, W., 2019. Efficient and practical Newton solvers for non-linear Stokes systems in geodynamic problems. *Geophysical Journal International*, *218*(2), pp.873-894.

26. Friedrich, A. M., Wernicke, B. P., Niemi, N. A., Bennett, R. A., & Davis, J. L. (2003). Comparison of geodetic and geologic data from the Wasatch region, Utah, and implications for the spectral character of Earth deformation at periods of 10 to 10 million years. *Journal of Geophysical Research: Solid Earth*, *108*(B4).
27. Friedrich, A.M., Wernicke, B.P., Niemi, N.A., Bennett, R.A. and Davis, J.L., 2003. Comparison of geodetic and geologic data from the Wasatch region, Utah, and implications for the spectral character of Earth deformation at periods of 10 to 10 million years. *Journal of Geophysical Research: Solid Earth*, *108*(B4).
28. Gleason, G.C. and Tullis, J., 1995. A flow law for dislocation creep of quartz aggregates determined with the molten salt cell. *Tectonophysics*, *247*(1-4), pp.1-23.
29. Glerum, A., Thieulot, C., Fraters, M., Blom, C. and Spakman, W., 2018. Nonlinear viscoplasticity in ASPECT: benchmarking and applications to subduction. *Solid Earth*, *9*(2), pp.267-294.
30. Goodall, H. J., Gregory, L. C., Wedmore, L. N. J., McCaffrey, K. J. W., Amey, R. M. J., Roberts, G. P., et al. (2021). Determining Histories of Slip on Normal Faults With Bedrock Scarps Using Cosmogenic Nuclide Exposure Data. *Tectonics*, *40*(3), e2020TC006457. https://doi.org/10.1029/2020TC006457
31. Goodall, H. J., Gregory, L. C., Wedmore, L. N., McCaffrey, K. J. W., Amey, R. M. J., Roberts, G. P., ... & Hooper, A. (2021). Determining histories of slip on normal faults with bedrock scarps using cosmogenic nuclide exposure data. *Tectonics*, *40*(3).
32. Gouiza, M., Naliboff, J. Rheological inheritance controls the formation of segmented rifted margins in cratonic lithosphere. *Nat Commun* 12, 4653 (2021). https://doi.org/10.1038/s41467-021-24945-5
33. Hamling, I.J., Hreinsdóttir, S., Clark, K., Elliott, J., Liang, C., Fielding, E., Litchfield, N., Villamor, P., Wallace, L., Wright, T.J. and D'Anastasio, E., 2017. Complex multifault rupture during the 2016 Mw 7.8 Kaikōura earthquake, New Zealand. *Science*, *356*(6334).
34. Heister, T., Dannberg, J., Gassmöller, R. and Bangerth, W., 2017. High accuracy mantle convection simulation through modern numerical methods–II: realistic models and problems. *Geophysical Journal International*, *210*(2), pp.833-851.
35. Hirth, G. and Kohlstedf, D., 2003. Rheology of the upper mantle and the mantle wedge: A view from the experimentalists. *Geophysical Monograph-American Geophysical Union*, *138*, pp.83-106.
36. Huismans, R.S. and Beaumont, C., 2007. Roles of lithospheric strain softening and heterogeneity in determining the geometry of rifts and continental margins. *Geological Society, London, Special Publications*, *282*(1), pp.111-138.
37. Iezzi, F., Mildon, Z., Walker, J.F., Roberts, G., Goodall, H., Wilkinson, M. and Robertson, J., 2018. Coseismic throw variation across along-strike bends on active normal faults: Implications for displacement versus length scaling of earthquake ruptures. *Journal of Geophysical Research: Solid Earth*, *123*(11), pp.9817-9841.

38. Jackson, C.A.L., Bell, R.E., Rotevatn, A. and Tvedt, A.B., 2017. Techniques to determine the kinematics of synsedimentary normal faults and implications for fault growth models. *Geological Society, London, Special Publications*, *439*(1), pp.187-217.
39. Kim, Y.S. and Sanderson, D.J., 2005. The relationship between displacement and length of faults: a review. *Earth-Science Reviews*, *68*(3-4), pp.317-334
40. Kronbichler, M., Heister, T. and Bangerth, W., 2012. High accuracy mantle convection simulation through modern numerical methods. *Geophysical Journal International*, *191*(1), pp.12-29.
41. Lavier, L.L., Buck, W.R. and Poliakov, A.N., 2000. Factors controlling normal fault offset in an ideal brittle layer. *Journal of Geophysical Research: Solid Earth*, *105*(B10), pp.23431-23442.
42. Manighetti, I., Zigone, D., Campillo, M., & Cotton, F. (2009). Self-similarity of the largest-scale segmentation of the faults: Implications for earthquake behavior. *Earth and Planetary Science Letters*, *288*(3-4), 370-381.
43. McLeod, A. E., Dawers*, N. H., & Underhill, J. R. (2000). The propagation and linkage of normal faults: insights from the Strathspey–Brent–Statfjord fault array, northern North Sea. *Basin Research*, *12*(3-4), 263-284.
44. Mechernich, S., Schneiderwind, S., Mason, J., Papanikolaou, I. D., Deligiannakis, G., Pallikarakis, A., ... & Reicherter, K. (2018). The seismic history of the Pisia fault (eastern Corinth rift, Greece) from fault plane weathering features and cosmogenic 36Cl dating. *Journal of Geophysical Research: Solid Earth*, *123*(5), 4266-4284.
45. Mechernich, S., Schneiderwind, S., Mason, J., Papanikolaou, I. D., Deligiannakis, G., Pallikarakis, A., et al. (2018). The Seismic History of the Pisia Fault (Eastern Corinth Rift, Greece) From Fault Plane Weathering Features and Cosmogenic 36Cl Dating. *J. Geophys. Res. Solid Earth*, *123*(5), 4266–4284. https://doi.org/10.1029/2017JB014600
46. Meyer, V., Nicol, A., Childs, C., Walsh, J. J., & Watterson, J. (2002). Progressive localisation of strain during the evolution of a normal fault population. *Journal of Structural Geology*, *24*(8), 1215-1231.
47. Mildon, Z. K., Roberts, G. P., Faure Walker, J. P., & Iezzi, F. (2017). Coulomb stress transfer and fault interaction over millennia on non-planar active normal faults: the M w 6.5–5.0 seismic sequence of 2016–2017, central Italy. *Geophysical Journal International*, *210*(2), 1206-1218.
48. Mitchell, S. G., Matmon, A., Bierman, P. R., Enzel, Y., Caffee, M., & Rizzo, D. (2001). Displacement history of a limestone normal fault scarp, northern Israel, from cosmogenic 36Cl. *Journal of Geophysical Research: Solid Earth*, *106*(B3), 4247-4264.
49. Morley, C. K. (1999). Patterns of displacement along large normal faults: implications for basin evolution and fault propagation, based on examples from East Africa. *AAPG bulletin*, *83*(4), 613-634.
50. Mouslopoulou, V., Walsh, J. J., & Nicol, A. (2009). Fault displacement rates on a range of timescales. *Earth and Planetary Science Letters*, *278*(3-4), 186-197.

51. Mouslopoulou, V., Walsh, J. J., & Nicol, A. (2009). Fault displacement rates over a range of timescales. Earth and Planetary Science Letters, 278, 186–197.
52. Naliboff, J.B., Glerum, A., Brune, S., Péron-Pinvidic, G. and Wrona, T., 2020. Development of 3-D rift heterogeneity through fault network evolution. *Geophysical Research Letters*, *47*(13), p.e2019GL086611.
53. Nicol, A., Mouslopoulou, V., Begg, J., Oncken, O. (2020): Displacement Accumulation and Sampling of Paleoearthquakes on Active Normal Faults of Crete in the Eastern Mediterranean. - Geochemistry Geophysics Geosystems (G3), 21, 11, e2020GC009265.
54. Nicol, A., Walsh, J. J., Watterson, J., & Underhill, J. R. (1997). Displacement rates of normal faults. *Nature*, *390*(6656), 157.
55. Nicol, A., Walsh, J., Berryman, K. and Villamor, P., 2006. Interdependence of fault displacement rates and paleoearthquakes in an active rift. *Geology*, *34*(10), pp.865-868.
56. Nicol, A., Walsh, J.J., Manzocchi, T. and Morewood, N., 2005. Displacement rates and average earthquake recurrence intervals on normal faults. *Journal of Structural Geology*, *27*(3), pp.541-551.
57. Nixon, C. W., McNeill, L. C., Bull, J. M., Bell, R. E., Gawthorpe, R. L., Henstock, T. J., ... & Kranis, H. (2016). Rapid spatiotemporal variations in rift structure during development of the Corinth Rift, central Greece. *Tectonics*, *35*(5), 1225-1248.
58. Oskin, M., Perg, L., Blumentritt, D., Mukhopadhyay, S. and Iriondo, A., 2007. Slip rate of the Calico fault: Implications for geologic versus geodetic rate discrepancy in the Eastern California Shear Zone. *Journal of Geophysical Research: Solid Earth*, *112*(B3).
59. Pan, S., Bell, R. E., Jackson, C. A. L., & Naliboff, J. (2020). Evolution of normal fault displacement and length as continental lithosphere stretches. *Basin Research*.
60. Phillips, T.B., Jackson, C.A., Bell, R.E., Duffy, O.B. and Fossen, H., 2016. Reactivation of intrabasement structures during rifting: A case study from offshore southern Norway. *Journal of Structural Geology*, *91*, pp.54-73.
61. Reeve, M. T., Bell, R. E., Duffy, O. B., Jackson, C. A. L., & Sansom, E. (2015). The growth of non-colinear normal fault systems; What can we learn from 3D seismic reflection data?. *Journal of Structural Geology*, *70*, 141-155.
62. Reeve, M., Bell, R., Duffy, O., Jackson, C. A.-L., & Sansom, E. (2015). The growth of non- colinear normal fault systems; What can we learn from 3D seismic reflection data? | Elsevier Enhanced Reader. *Journal of Structural Geology*, *70*. https://doi.org/10.1016/j.jsg.2014.11.007
63. Roberts, G.P. and Michetti, A.M., 2004. Spatial and temporal variations in growth rates along active normal fault systems: an example from The Lazio–Abruzzo Apennines, central Italy. *Journal of Structural Geology*, *26*(2), pp.339-376.
64. Roberts, G.P. and Michetti, A.M., 2004. Spatial and temporal variations in growth rates along active normal fault systems: an example from The Lazio–Abruzzo Apennines, central Italy. *Journal of Structural Geology*, *26*(2), pp.339-376.

65. Rose, I., Buffett, B. and Heister, T., 2017. Stability and accuracy of free surface time integration in viscous flows. *Physics of the Earth and Planetary Interiors*, *262*, pp.90-100.
66. Rotevatn, A., Jackson, C.A.L., Tvedt, A.B., Bell, R.E. and Blækkan, I., 2019. How do normal faults grow?. *Journal of Structural Geology*, *125*, pp.174-184.
67. Rybacki, E., Gottschalk, M., Wirth, R. and Dresen, G., 2006. Influence of water fugacity and activation volume on the flow properties of fine-grained anorthite aggregates. *Journal of Geophysical Research: Solid Earth*, *111*(B3).
68. Schlagenhauf, A., Manighetti, I., Malavieille, J. and Dominguez, S., 2008. Incremental growth of normal faults: Insights from a laser-equipped analog experiment. *Earth and Planetary Science Letters*, *273*(3-4), pp.299-311.
69. Segall, P., & Pollard, D. D. (1980). Mechanics of discontinuous faults. *Journal of Geophysical Research: Solid Earth*, *85*(B8), 4337-4350.
70. Shillington, D. J., Scholz, C. A., Chindandali, P. R., Gaherty, J. B., Accardo, N. J., Onyango, E., ... & Nyblade, A. A. (2020). Controls on Rift Faulting in the North Basin of the Malawi (Nyasa) Rift, East Africa. *Tectonics*, *39*(3), e2019TC005633.
71. Stein, R.S., 1999. The role of stress transfer in earthquake occurrence. *Nature*, *402*(6762), pp.605-609.
72. Taylor, S.K., Bull, J.M., Lamarche, G. and Barnes, P.M., 2004. Normal fault growth and linkage in the Whakatane Graben, New Zealand, during the last 1.3 Myr. *Journal of Geophysical Research: Solid Earth*, *109*(B2)
73. Thieulot, C., 2011. FANTOM: Two-and three-dimensional numerical modelling of creeping flows for the solution of geological problems. *Physics of the Earth and Planetary Interiors*, *188*(1-2), pp.47-68.
74. Van Dinther, Y., Gerya, T.V., Dalguer, L.A., Corbi, F., Funiciello, F. and Mai, P.M., 2013. The seismic cycle at subduction thrusts: 2. Dynamic implications of geodynamic simulations validated with laboratory models. *Journal of Geophysical Research: Solid Earth*, *118*(4), pp.1502-1525.
75. Van Wijk, J. W., & Cloetingh, S. A. P. L. (2002). Basin migration caused by slow lithospheric extension. *Earth and Planetary Science Letters*, *198*(3-4), 275-288.
76. Walker, J. F., Boncio, P., Pace, B., Roberts, G., Benedetti, L., Scotti, O., ... & Peruzza, L. (2021). Fault2SHA Central Apennines database and structuring active fault data for seismic hazard assessment. *Scientific data*, *8*(1), 1-20.
77. Walker, J.F., Roberts, G.P., Cowie, P.A., Papanikolaou, I.D., Sammonds, P.R., Michetti, A.M. and Phillips, R.J., 2009. Horizontal strain-rates and throw-rates across breached relay zones, central Italy: Implications for the preservation of throw deficits at points of normal fault linkage. *Journal of Structural Geology*, *31*(10), pp.1145-1160.
78. Wallace, L.M., Ellis, S., Miyao, K., Miura, S., Beavan, J. and Goto, J., 2009. Enigmatic, highly active left-lateral shear zone in southwest Japan explained by aseismic ridge collision. *Geology*, *37*(2), pp.143-146.

79. Wallace, R. E. (1987). Grouping and migration of surface faulting and variations in slip rates on faults in the Great Basin province. *Bulletin of the Seismological Society of America*, *77*(3), 868-876.
80. Walsh, J.J. and Watterson, J., 1988. Analysis of the relationship between displacements and dimensions of faults. *Journal of Structural geology*, *10*(3), pp.239-247.
81. Walsh, J.J., Nicol, A. and Childs, C., 2002. An alternative model for the growth of faults. *Journal of Structural Geology*, *24*(11), pp.1669-1675.
82. Walters, R.J., Gregory, L.C., Wedmore, L.N., Craig, T.J., McCaffrey, K., Wilkinson, M., Chen, J., Li, Z., Elliott, J.R., Goodall, H. and Iezzi, F., 2018. Dual control of fault intersections on stop-start rupture in the 2016 Central Italy seismic sequence. *Earth and Planetary Science Letters*, *500*, pp.1-14.
83. Wedmore, L. N., Biggs, J., Williams, J. N., Fagereng, Å., Dulanya, Z., Mphepo, F., & Mdala, H. (2020). Active fault scarps in southern Malawi and their implications for the distribution of strain in incipient continental rifts. *Tectonics*, *39*(3), e2019TC005834.
84. Weldon, R., Scharer, K., Fumal, T., & Biasi, G. (2004). Wrightwood and the earthquake cycle: What a long recurrence record tells us about how faults work. *GSA today*, *14*(9), 4-10.
85. Wells, D.L. and Coppersmith, K.J., 1994. New empirical relationships among magnitude, rupture length, rupture width, rupture area, and surface displacement. *Bulletin of the seismological Society of America*, *84*(4), pp.974-1002.
86. Wesnousky, S. G. (2008). Displacement and geometrical characteristics of earthquake surface ruptures: Issues and implications for seismic-hazard analysis and the process of earthquake rupture. *Bull. Seismol. Soc. Am.*, *98*(4), 1609–1632. https://doi.org/10.1785/0120070111
87. Worldwide and Unified Database of Surface Ruptures (SURE) for Fault Displacement Hazard Analyses. *Seismological Research Letters*, *91*(1), 499–520. https://doi.org/10.1785/0220190144

Fig. 1. (a) Continental extension model setup outlining initial boundary conditions, compositional layers and prescribed initial strain. Resolution is progressively refined to higher levels up to 650 m in the model centre (180 x 180 x 20 km region), where we perform fault extraction analysis at 5 km beneath the initial model surface (e.g., 95 km above the model base). **(b)** Strain rate second invariant (1/s) after 100 kyrs, cropped to the centered 650 m resolution zone. The deformation patterns reveal that the randomised initial plastic strain field produces rapid localisation of a well-defined normal fault network.

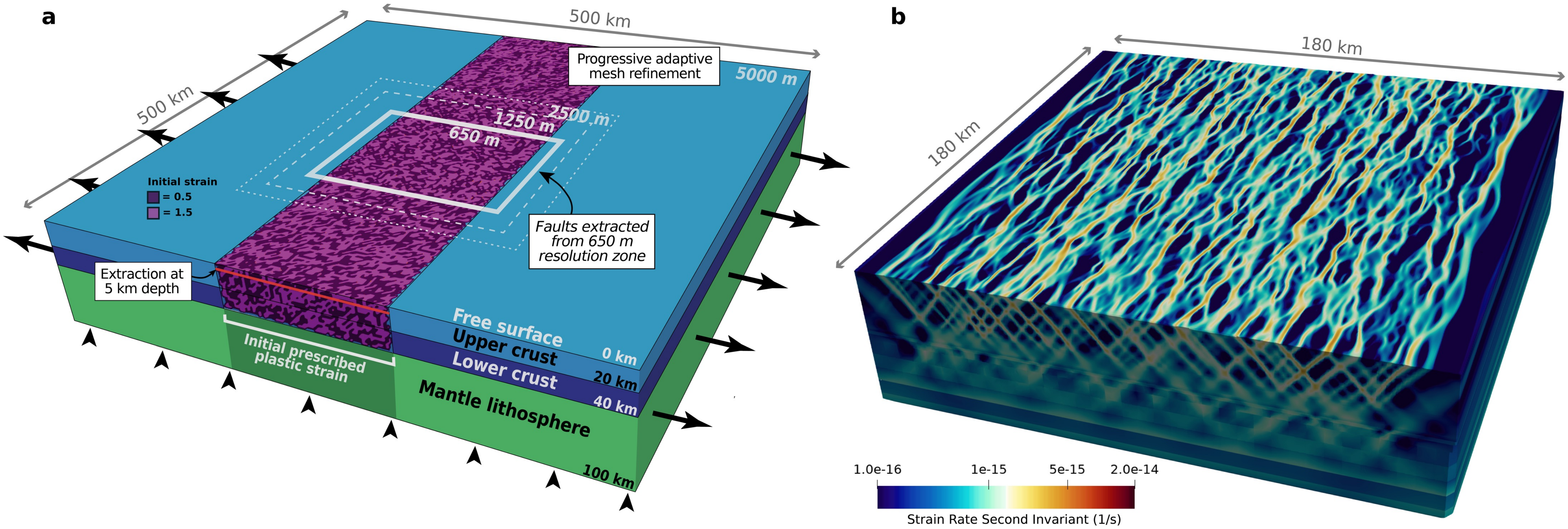

Fig. 2. Conventional image processing techniques, which here are derived from the strain rate field 5 km below the initial model surface. This approach performs a binay threshold, where values below a specified cutoff point (3e-15 and 1-e15 1/s) are assigned 0 and values above are assigned 1 (**b** and **e**). Regions which are connected in the binary threshold are grouped into components labelled as integers (**c** and **f**). However, a high cutoff value does not capture small scale strain and makes fundamental assumptions on the resulting fault length (**c**). In contrast, a low cutoff value results in labels containing multiple fault segments, in which length cannot be extracted (**f**). **Details and examples of this fault extraction procedure are provided in the supplementary materials.**

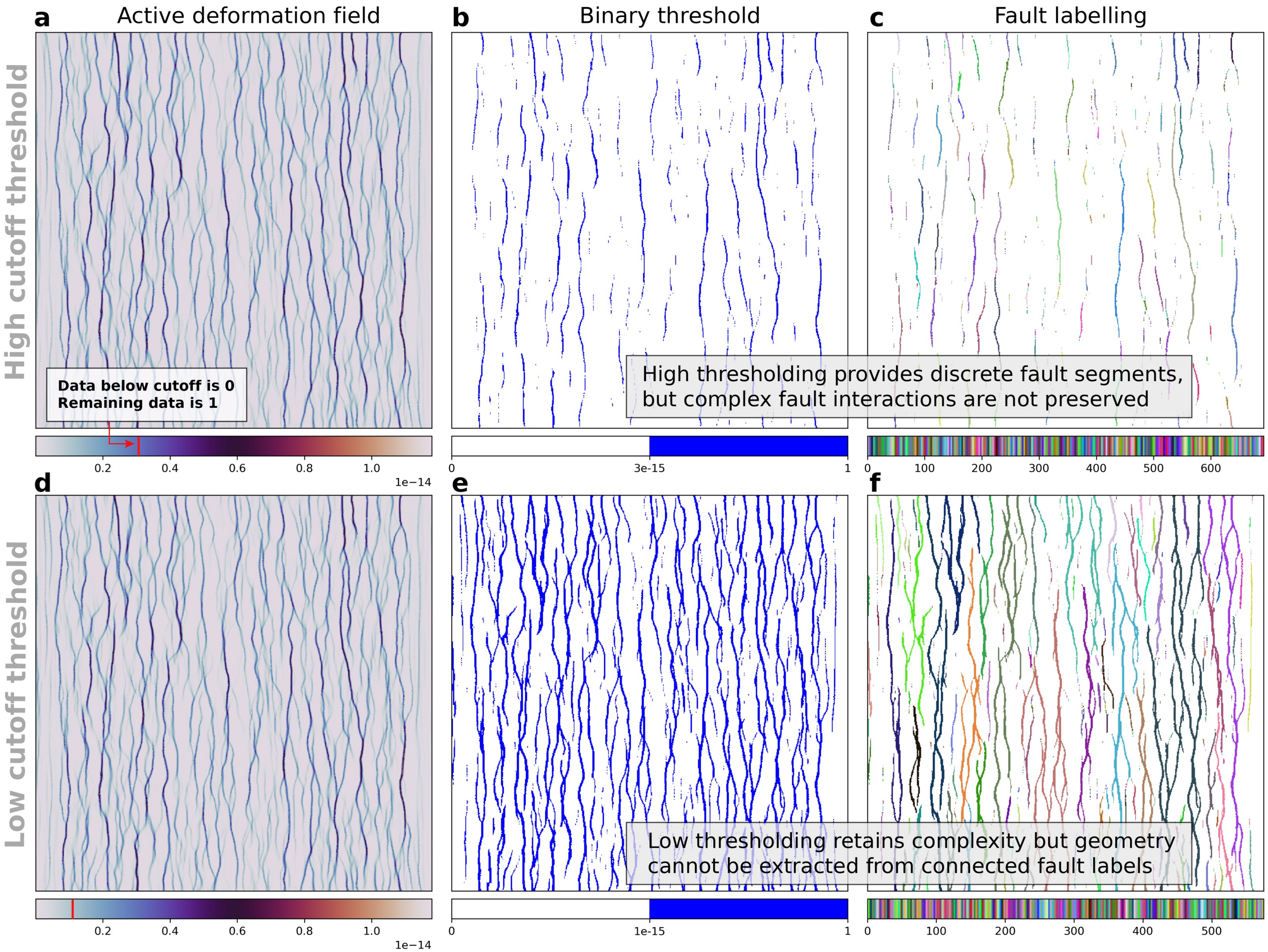

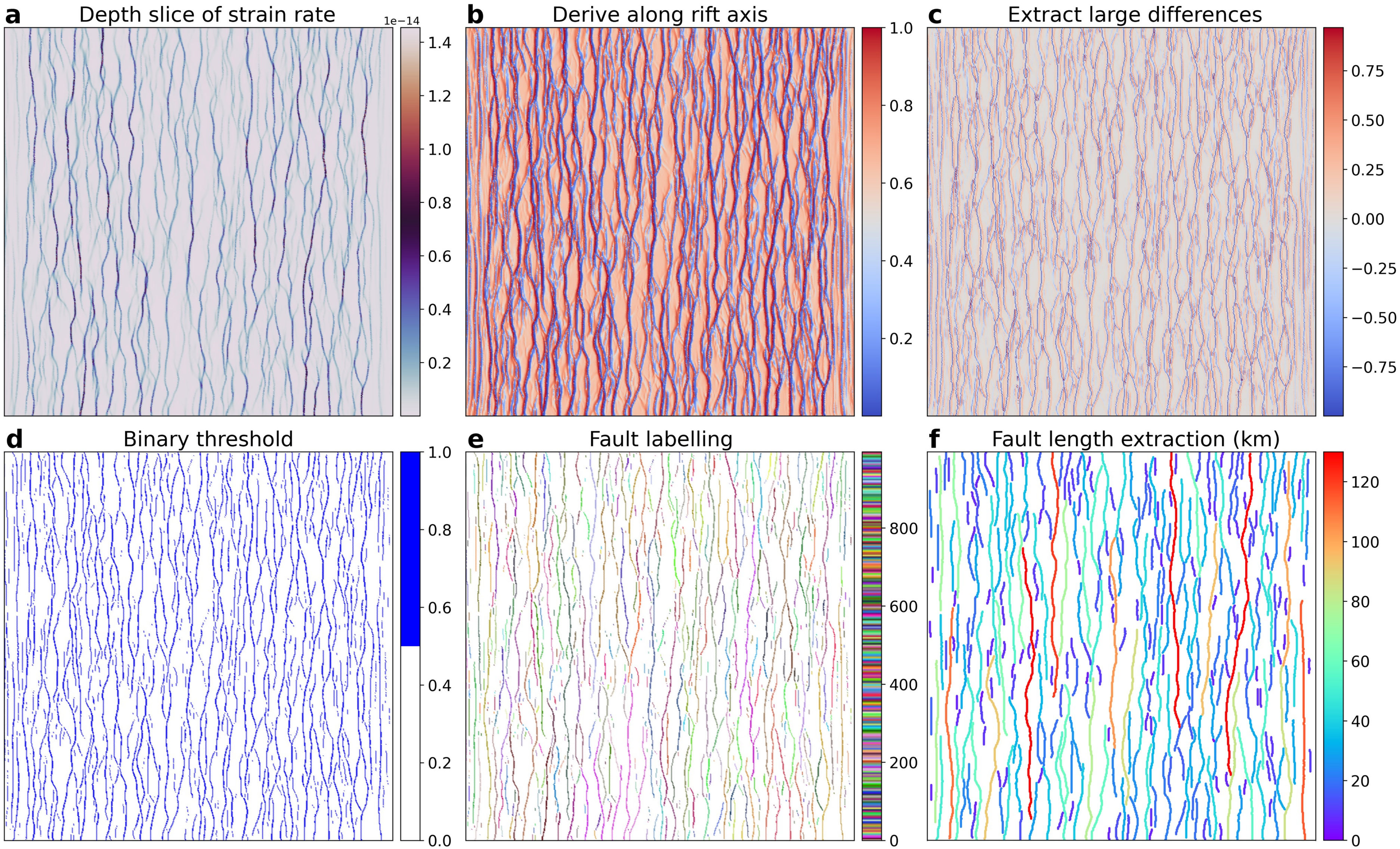

Fig. 3. Novel fault extraction workflow. The active deformation field (e.g., second strain invariant) is extracted 5 km below the initial model surface (a). The spatial derivative of the second strain invariant in the along-strike direction (e.g., z-direction) is calculated, and the resulting field is equalised to 0-1 showing that values of 0 and 1 lie on the sides of fault localities **(b)**. An across-strike derivation **(c)** identifies these localities, in which a binary threshold is applied **(d)**. Spatially connected regions of the binary array are labelled as integers **(e)** and noise is removed. This method results in the extraction of discrete fault segments, such that fault length may be derived **(f)**.

Fig. 4. Active deformation (left) and accumulated brittle plastic deformation (right) for the model extending a constant rate of 5 mm yr^{-1}, after 1 Myrs (**a** and **b**) and 5 Myrs (**c** and **d**) of extension. The second strain rate invariant (1/s) on the left, documenting active deformation, are limited to values above 1e-16 here to better reveal and compare the main active structures. At 1 Myr, deformation is relatively distributed across faults whereas at 5 Myrs structures are localised onto the largest faults. See Supplementary Video 1 for animation across all modelled timesteps.

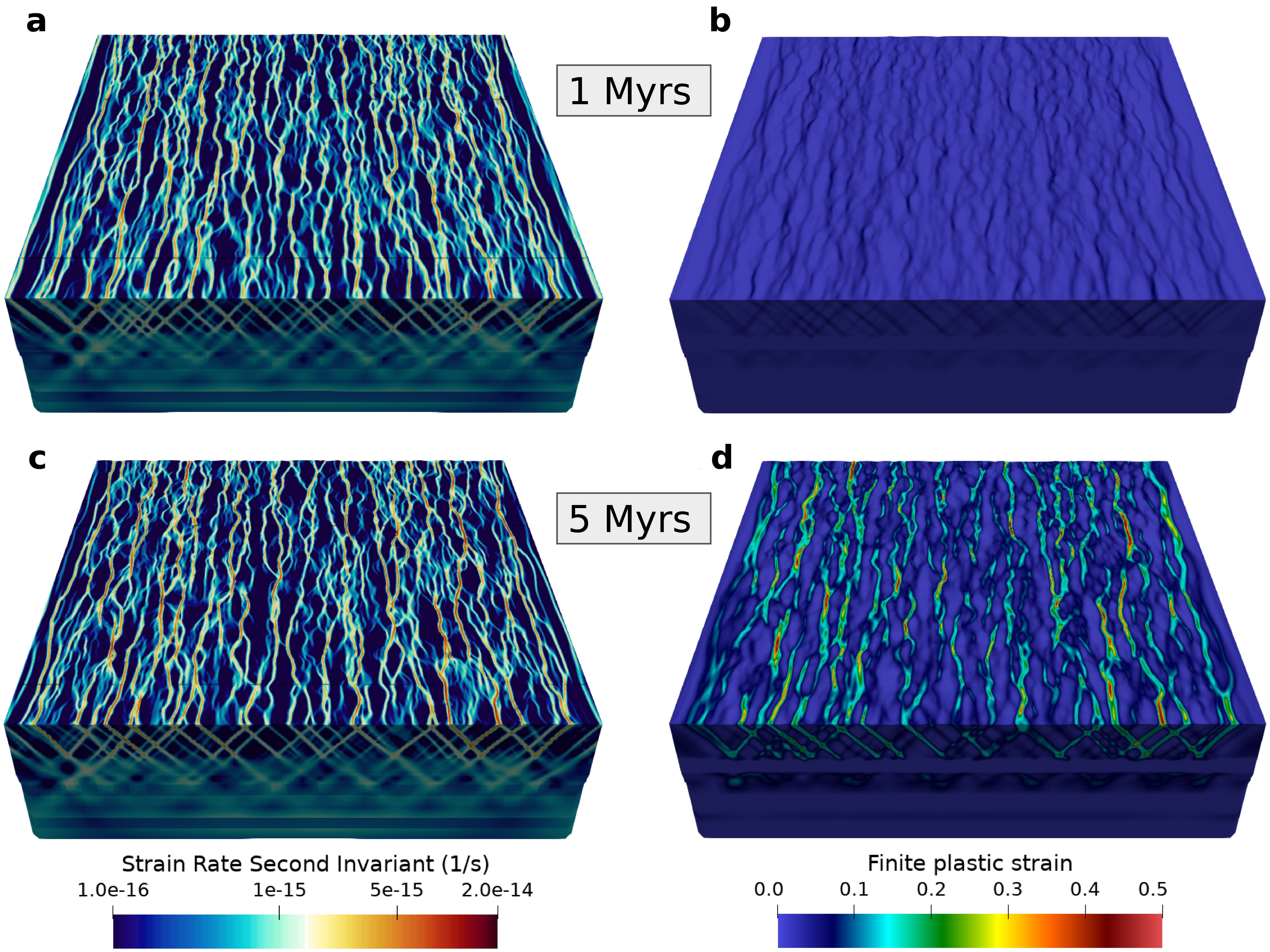

Fig. 5. Comparison across models with extension rates of 2.5, 5, and 10 mm yr^{-1}. The top row shows the strain rate invariant (s^{-1}) in the upper crust (extracted at 5 km depth), documenting active deformation patterns within the last resolvable time increment (50) representing 10, 5 and 2.5 Myrs extension, respectively. The bottom row shows their corresponding fault length extracted from the active deformation field. See Supplementary Video 2 for animation across all modelled timesteps.

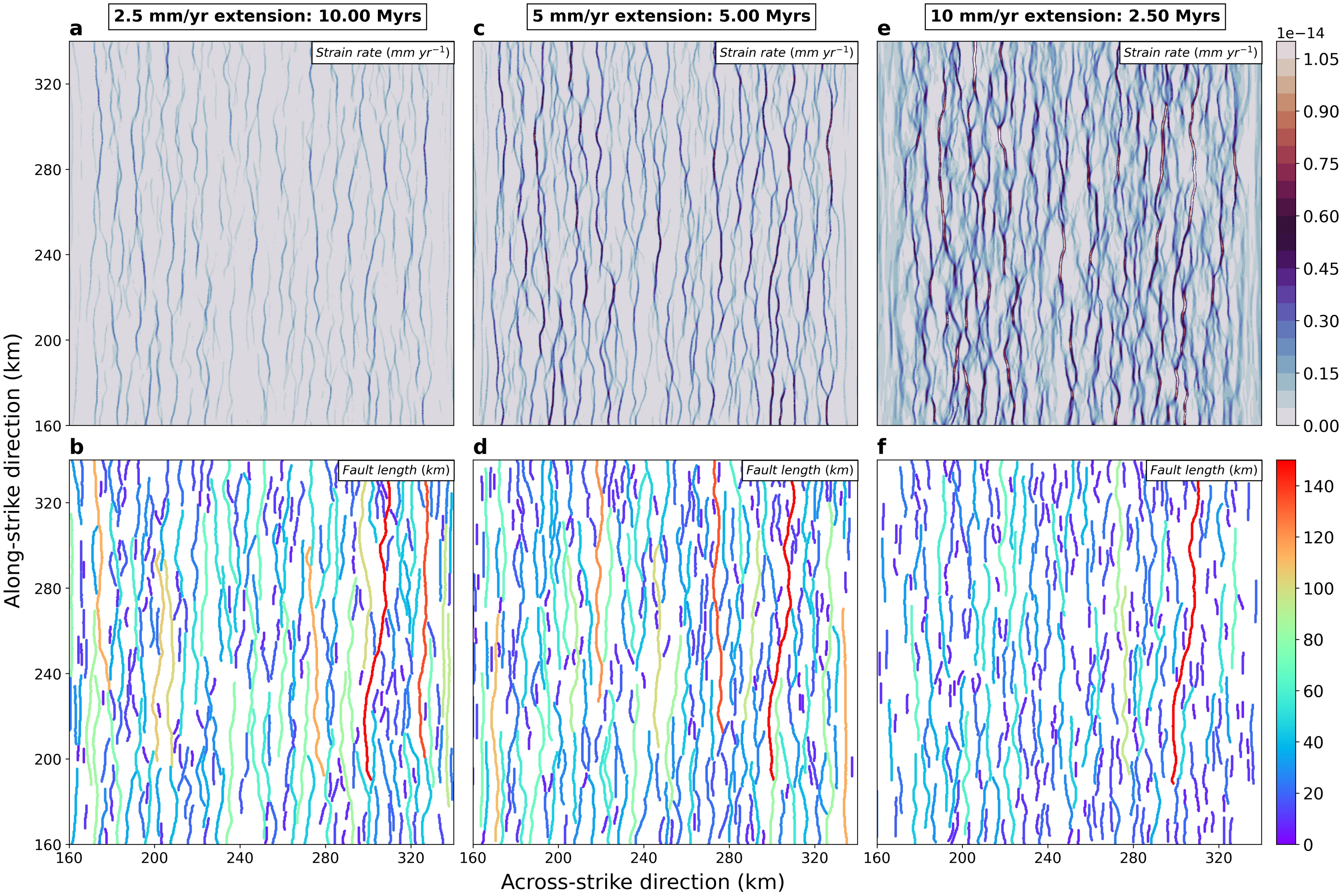

Fig. 6. Fault D-L evolution for the modelled fault network extending at a rate of 5 mm yr^{-1}. Observational datasets are plotted in grey, where different shades correlate to references therein, and the modelled data are in colour. See Supplementary Video 3 for animation across all modelled timesteps.

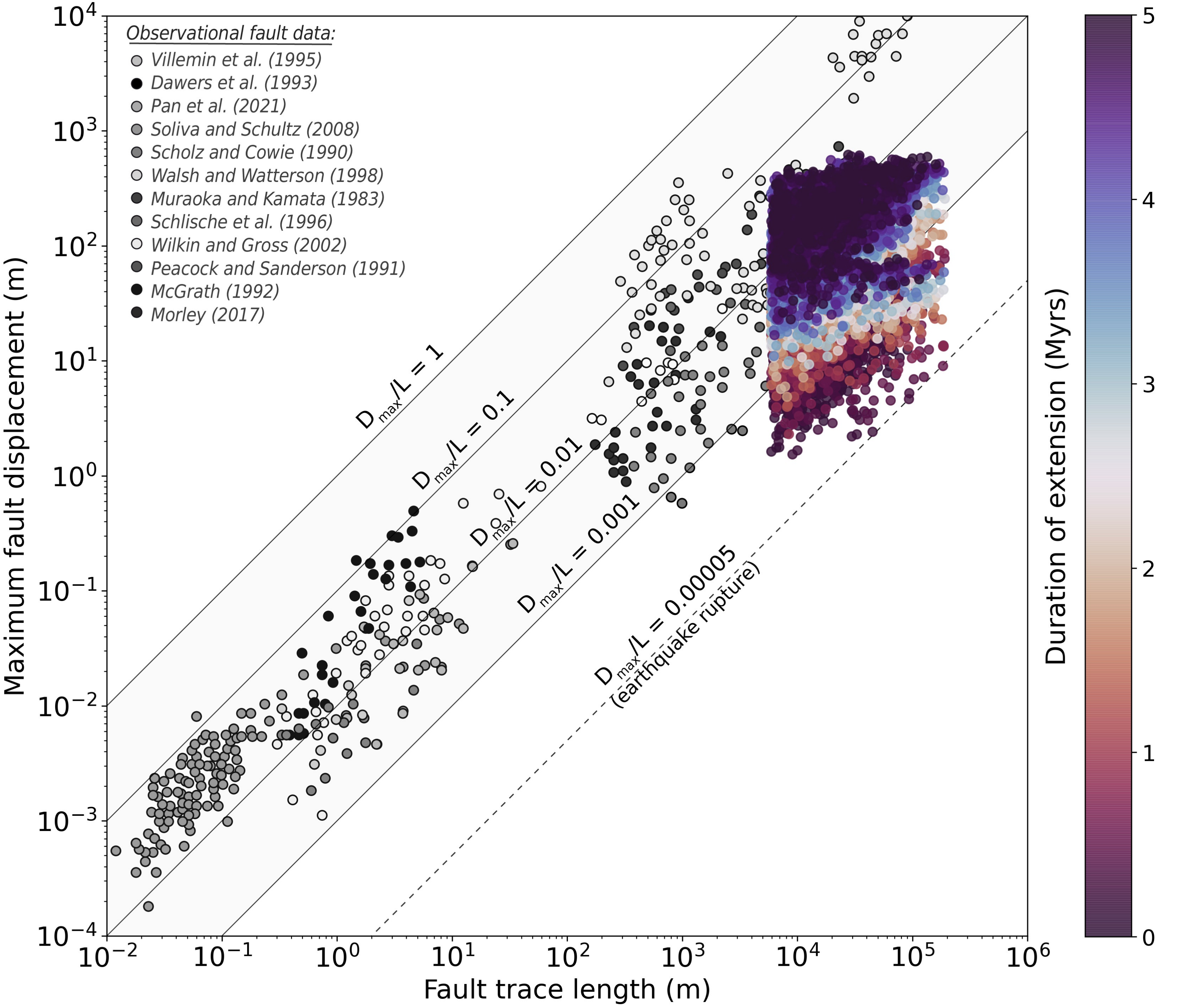

Fig. 7. Geometric statistics of time-dependent fault properties. (**a**) The number of active faults through time. **(b)** The average active fault length through time. Note that while the plot contains all output timesteps for each model (50 total), however the total duration for models deformed at 2.5, 5 and 10 mm yr^{-1} are 10, 5 and 2.5 Myrs, respectively. As such, each timestep along the horizontal axis corresponds to an equivalent amount of total extension experienced by each model, rather than the same model time.

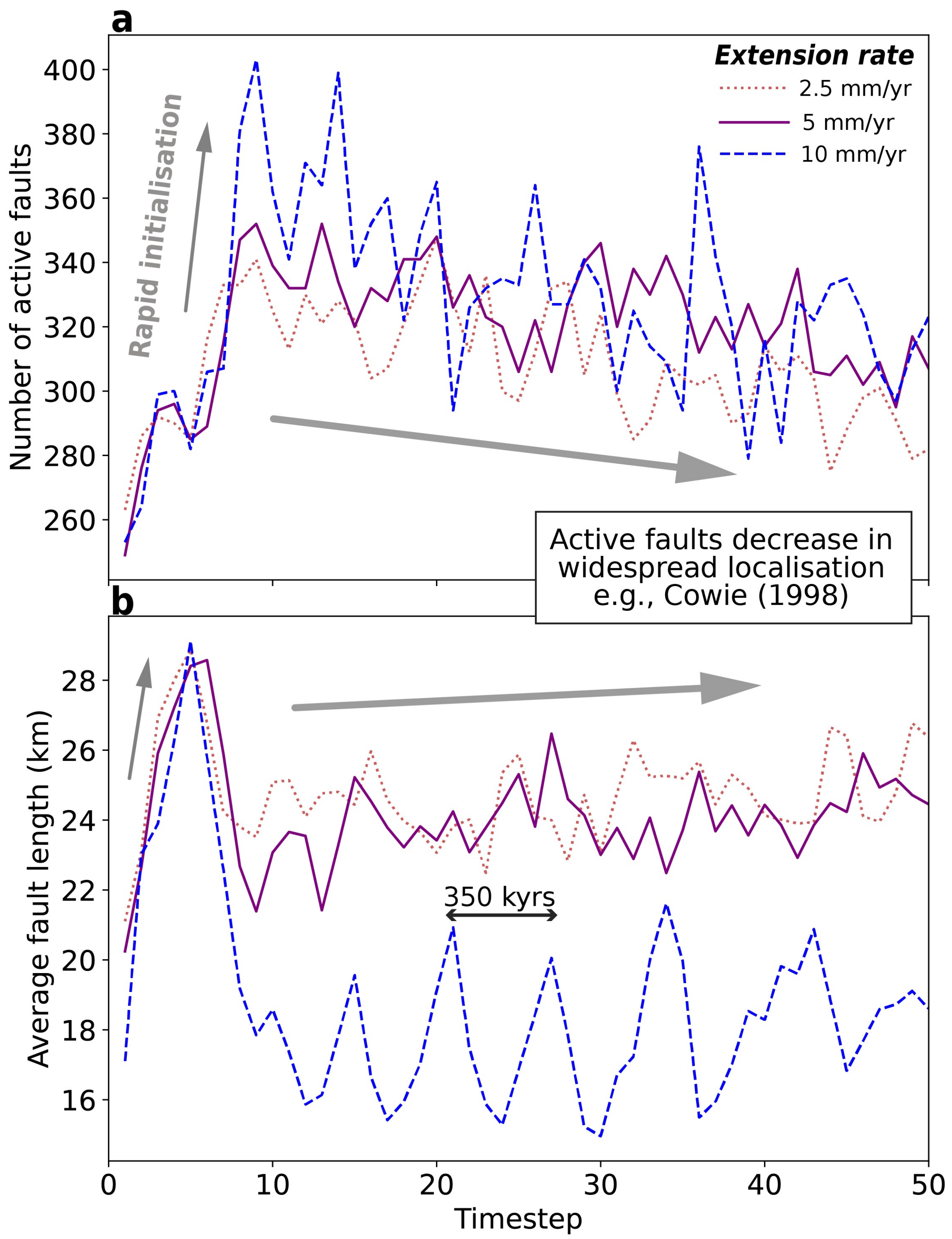

Fig. 8. End-member behaviour of transient deformation. Along-strike maps from a subset of the model that experienced 10 mm yr^{-1} extension. The strain rate second invariant **(a)**, finite strain (plastic strain invariant) **(b)**, and extracted faults **(c)** at 2.1 Myrs reveal localised, continuous behaviour. The strain rate second invariant **(d)**, finite strain **(e)** and extracted faults **(f)** at 2.2 Myrs reveal distributed, segmented behaviour.